analytical chemistry

pubs.acs.org/ac Article

Microneedle Aptamer-Based Sensors for Continuous, Real-Time Therapeutic Drug Monitoring

Yao Wu, Farshad Tehrani, Hazhir Teymourian, John Mack, Alexander Shaver, Maria Reynoso, Jonathan Kavner, Nickey Huang, Allison Furmidge, Andrés Duvvuri, Yuhang Nie, Lori M. Laffel, Francis J. Doyle III, Mary-Elizabeth Patti, Eyal Dassau, Joseph Wang,* and Netzahualcóyotl Arroyo-Currás*

Cite This: *Anal. Chem.* 2022, 94, 8335−8345 Read Online

ACCESS | Metrics & More | Article Recommendations | Supporting Information

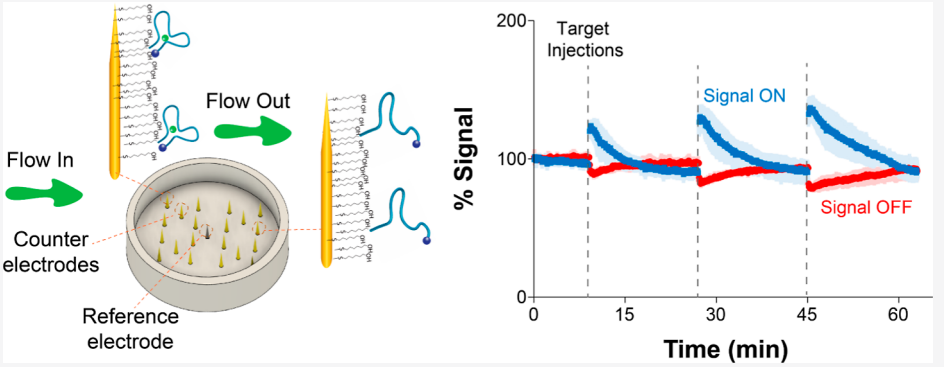

ABSTRACT: The ability to continuously monitor the concentration of specific molecules in the body is a long-sought goal of biomedical research. For this purpose, interstitial fluid (ISF) was proposed as the ideal target biofluid because its composition can rapidly equilibrate with that of systemic blood, allowing the assessment of molecular concentrations that reflect full-body physiology. In the past, continuous monitoring in ISF was enabled by microneedle sensor arrays. Yet, benchmark microneedle sensors can only detect molecules that undergo redox reactions, which limits the ability to sense metabolites, biomarkers, and therapeutics that are not redox-active. To overcome this barrier, here, we expand the scope of these devices by demonstrating the first use of microneedle-supported electrochemical, aptamer-based (E-AB) sensors. This platform achieves molecular recognition based on affinity interactions, vastly expanding the scope of molecules that can be sensed. We report the fabrication of microneedle E-AB sensor arrays and a method to regenerate them for multiple uses. In addition, we demonstrate continuous molecular measurements using these sensors in flow systems in vitro using single and multiplexed microneedle array configurations. Translation of the platform to in vivo measurements is possible as we demonstrate with a first E-AB measurement in the ISF of a rodent. The encouraging results reported in this work should serve as the basis for future translation of microneedle E-AB sensor arrays to biomedical research in preclinical animal models.

The development of wearable and autonomous sensing technologies enabling continuous, real-time monitoring of clinically relevant therapeutics, metabolites, and biomarkers in the body could dramatically transform the way we study, understand, diagnose, and treat diseases. Such technologies could be used to, for example, achieve highly precise and personalized drug therapy via real-time monitoring of patient-specific pharmacokinetics, pharmacodynamics, and toxicology.[1−6] The in vivo pharmacological data produced could be coupled to drug delivery devices via feedback control, allowing therapeutic dosing to occur at the exact time and dose needed and in response to minute-to-minute fluctuations in an individual's physiology.[7−9] In contrast, our current approach to drug therapy often relies on population-based physical indexes such as age, weight, or body mass, which are often inaccurate at the individual's level, or indirect parameters such as genotype, which are poor predictors of a patient's immediate physiological state and of effective therapeutic dosing.[10,11] In addition, the standard of care for using phlebotomy and laboratory-based molecular measurements is costly, slow, and inconvenient.[12,13] Given the clinical importance of developing

Received: February 20, 2022
Accepted: May 19, 2022
Published: June 2, 2022

https://doi.org/10.1021/acs.analchem.2c00829
Anal. Chem. 2022, 94, 8335−8345

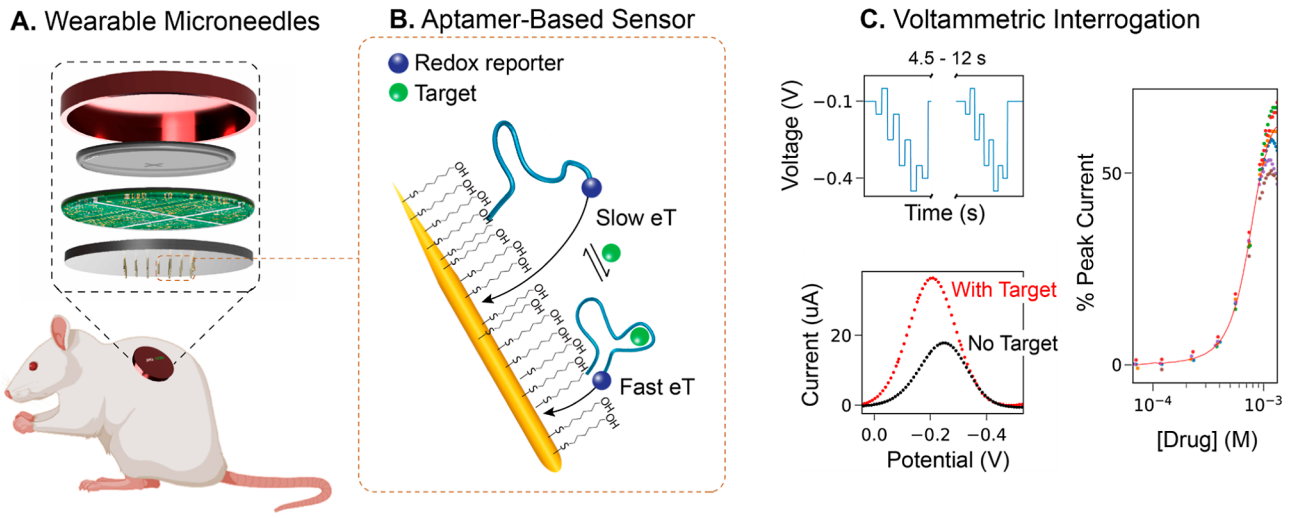

Figure 1. Wearable microneedle aptamer-based sensors for continuous, real-time therapeutic drug monitoring. (A) Our wearable microneedle sensor patch is designed to allow painless on-body molecular tracking in research animals. The patch consists of a microneedle sensor array integrated with electronics and a battery, all contained within a wearable case. The sensor array contains 16 gold working, 4 platinum counter, and one central reference microneedles with a form factor that allows painless penetration of the upper strata of the reticular dermis. (B) At the core of our sensing technology are electrochemical aptamer-based (E-AB) sensors, which consist of a mixed self-assembled monolayer of electrode-blocking alkanethiols with alkanethiol- and redox reporter-modified aptamers. In the presence of a target, the aptamers undergo reversible binding-induced conformational changes that affect electron transfer (eT) between the reporter and the gold needles. This sensing mechanism is reversible. (C) To enable continuous drug monitoring, the sensors are serially interrogated by square-wave voltammetry (SWV) with a time interval between 4.5 and 12 s. The sensors can be calibrated at the point of manufacture by building target titration curves, allowing correlation of current changes to changes in target concentration.

therapeutic strategies that effectively address patient-to-patient pharmacokinetic variability[14] and overcome inaccurate pharmacokinetic estimates,[15] there remains a critical need for in vivo sensing platforms that can achieve autonomous, continuous, and individualized molecular monitoring in real time.

The future of personalized medicine will almost certainly involve some form of wearable biochemical monitors. In this context, interstitial fluid (ISF) is an ideal compartment for monitoring systemic molecular levels as it presents biomolecular concentrations and temporal, dynamic profiles that strongly correlate with those of blood.[16,17] For example, continuous glucose monitors have successfully used ISF glucose levels as a proxy for blood glucose concentration.[18] However, the biologic diversity of ISF means that there is ample opportunity to leverage this fluid for molecular monitoring of other clinically important targets, both in continuous or semicontinuous modes. The fact that ISF is immediately available under the outermost layers of the skin makes it an ideal target for minimally invasive and painless technologies for wearable molecular monitors.

A much-highlighted strategy to access ISF without any perceivable pain or skin damage is the use of wearable microneedles.[19,20] By virtue of their sharp microscopic structures, microneedles can pierce the stratum corneum of the skin and reach the ISF within the dermis. Thanks to their shallow depth (∼1 mm), microneedles reach neither nerve endings nor vasculature within the dermis,[19] offering painless and direct tapping into the ISF. To date, this technology has been used to achieve high-volume extraction of ISF for in vitro proteomics,[20] controlled therapeutic delivery,[21,22] and molecular monitoring using microneedle-supported biosensors.[23−25] However, successes in continuous sensing have been limited to a few molecules that either undergo enzymatic conversion via oxidases or reductases[23,24,26,27] or are redox-active and can be directly oxidized or reduced on microneedle surfaces.[28] Thus, there remains a critical need to develop methods that expand the scope of microneedle-supported sensing to health-relevant ISF markers that cannot undergo enzymatic or direct electrochemical conversion.

This work aims to expand the sensing scope of microneedle sensors by coupling the technology with electrochemical, aptamer-based (E-AB) sensors (Figure 1), an affinity-based measurement strategy that does not depend on molecular reactivity.[29] Aptamers are single-stranded nucleic acid sequences that can be selected through systematic evolution of ligands by exponential enrichment (SELEX) for binding to arbitrary targets with high affinity.[30−32] For example, taking advantage of endotoxin-binding aptamers and porous microneedle arrays, Yi et al.[33] achieved extraction of ISF and ex vivo detection of endotoxin based on fluorescence emission. Although these aptamer-decorated porous microneedles enable the extraction and ex vivo detection of biomarkers in ISF, they cannot support continuous, real-time molecular monitoring in vivo. Similarly, the use of immunoassays for expanding the molecular scope of microneedles is hindered by the inability to regenerate the antibody receptor. However, such challenges can be resolved by coupling the high affinity and reversible molecular recognition afforded by aptamers with real-time electrochemical detection. Specifically, the aptamers in E-AB sensors undergo binding-induced conformational changes (Figure 1B),[34] which occur in scales of milliseconds and are reversible. The aptamers are modified with redox reporters that undergo eT at different rates depending on the target concentration. By interrogating the sensors serially using voltammetry (Figure 1C), the platform supports continuous molecular monitoring with second[3] or subsecond[9] resolution both in vitro and in vivo.[3] More detailed descriptions of the working principle of E-AB sensors abound in the published literature. For example, we refer the reader to refs 35 and 36.

https://doi.org/10.1021/acs.analchem.2c00829
Anal. Chem. 2022, 94, 8335−8345

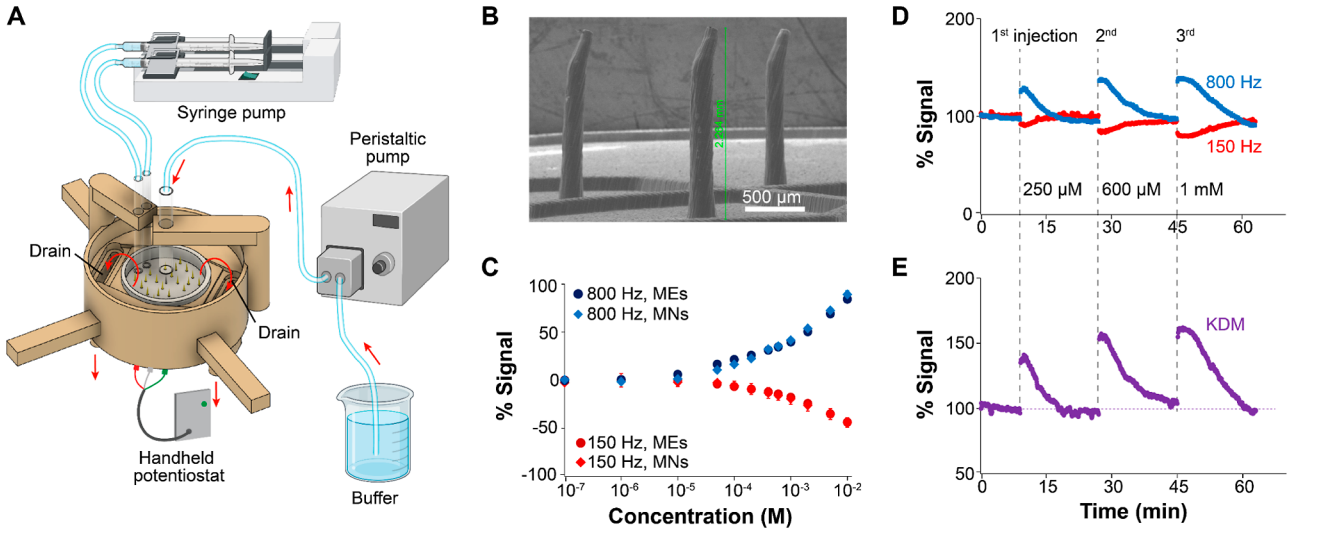

Figure 2. Microneedle E-AB sensor arrays support real-time molecular monitoring in vitro. (A) 3D-printed flow cell for continuous molecular monitoring. The microneedle sensor array is glued at the bottom of the cell and connected to a hand-held potentiostat to enable serial electrochemical interrogation. (B) Micrograph showing blunt microneedles used for rapid testing. The microneedle height is ∼2.3 mm, and the diameter ∼170 μm. We functionalized these using tobramycin-binding aptamers, which are modified to have covalently attached alkanethiol linkers and the redox reporter methylene blue. (C) Microneedle E-AB sensor arrays (MNs) achieve identical calibration curves relative to sensors fabricated on commercial disc macroelectrodes (MEs, 2 mm in diameter). Circles represent the average of six sensors fabricated on MEs; diamonds represent the average of three sensors fabricated on MNs; error bars represent their standard deviation. (D) Continuous, real-time monitoring of tobramycin in the flow system. Voltammetric measurements were performed every 4.5 s in 20 mM Tris, 100 mM NaCl, 5 mM $MgCl_2$ (pH = 7.4). (E) Kinetic differential measurements (KDM) obtained after subtracting the data collected at 150 Hz (signal-off output) from data collected at 800 Hz (signal-on output).

Here, we report the first microneedle E-AB sensor arrays for continuous monitoring of therapeutic agents. Specifically, this work reports five key innovations: (1) the design and manufacture of gold microneedle sensors (Figure 1A) that enable E-AB functionalization (Figure 1B) using established methods; (2) 3D-printed fluidic devices that mimic in vivo excretion kinetics to demonstrate that microneedle E-AB arrays achieve continuous drug monitoring in real time; (3) a cleaning protocol to successfully regenerate the surfaces of these highly engineered microneedles to enable reuse; (4) multiplexed monitoring of a prodrug and its metabolite at neighboring microneedles within the same array using a newly reported aptamer; and (5) preliminary deployment of this continuous E-AB monitor for real-time drug tracking in the ISF of one rodent.

EXPERIMENTAL SECTION

Expanded Methods are provided as the Supporting Information. The main procedures are described in brief below:

Microneedle Preparation. Microneedle electrodes for in vitro experiments were fabricated via 3D printing using a Formlabs 3D printer. Microneedle arrays for in vivo experiments were fabricated using CNC micromachining techniques and poly(methyl methacrylate) materials. We sputtered the microneedles with chromium-supported layers of chromium for 1 min at 100 W (chromium) and gold for 16 min at 100 W.

Microneedle Cleaning Protocol. We incubated newly fabricated microneedle devices in pure ethanol for 10 min, followed by electrochemical cleaning, as described in the Supporting Information under Macroelectrode Cleaning. This step removes gold oxides remaining from the fabrication process.[37] To ensure that gold oxides are removed completely, we repeated the same steps three times. Second, we immersed the microneedles in 600 μL of a 10% commercial gold cleaning solution in water for 10 s (SIGMA #667978). We then measured cyclic voltammograms at a scan rate of 100 mV/s in 0.05 M H_2SO_4 after each treatment to evaluate the cleanliness and gold area of the microneedles. The resulting voltammograms after each treatment (Figure S1) show that our protocol is effective at cleaning the needles while preventing the loss of sputtered gold.

Sensor Preparation. To prepare E-AB sensors, we first incubated 1 μL of 100 μM thiolated MB-modified DNA with 1 μL of 100 mM tris(2-carboxyethyl)phosphine to reduce disulfide bonds for 1 h. We then incubated working electrodes in the reduced DNA solution for 1 h, followed by a 3 h-long incubation in 30 mM mercaptohexanol at room temperature to force out nonspecifically absorbed probes. All buffers used for sensor preparation are described in the Supporting Information under Expanded Methods. All aptamer solutions were diluted to a final concentration of 200 nM prior to electrode functionalization, which was measured via UV−vis spectroscopy employing an Implen Nanophotometer NP80 (Westlake Village, CA). Sensor calibration procedures are described in the Supporting Information under the Expanded Methods section.

Electrochemical Measurements. A CH Instruments Electrochemical Analyzers (CHI 1040C, Austin, TX) multichannel potentiostat, (CHI 1242, Austin, TX) hand-held potentiostat, and associated software were used for all CV and SWV measurements. We used a three-electrode cell configuration consisting of gold disk working, platinum wire counter, and Ag/AgCl (saturated KCl) reference electrodes. CV measurements were recorded at a scan rate of 100 mV/s for evaluating the cleanliness and gold area of macroelectrodes and microneedles. SWV measurements were performed with a square-wave amplitude of 25 mV, a step size of 1 mV, and various frequencies.

https://doi.org/10.1021/acs.analchem.2c00829
Anal. Chem. 2022, 94, 8335−8345

In Vivo Measurements. Adult male Sprague-Dawley rats (300−500 g; Charles River Laboratories, Wilmington, MA, USA) were housed in a temperature-controlled vivarium on a 12 h light−dark cycle and provided ad libitum access to food and water. All animal procedures were consistent with the guidelines of the NIH Guide for Care and Use of Laboratory Animals and approved by the Institutional Animal Care and Use Committee of the Johns Hopkins University School of Medicine.

Microneedle sensor arrays were placed on the rat abdomen after shaving them using a store-bought razor to remove all fur in the area. We pressed and released the arrays 5× to ensure penetration of the microneedles into the skin and then taped them in place for the remainder of the experiment. Once a 30−60 min sensor baseline was established, we slowly infused 0.1 mL of tobramycin sulfate (100 mM, Spectrum Pharmacy Products, New Brunswick, NJ) through a vein catheter. Recordings were taken for 1 h following drug infusions. The real-time plotting and analysis of voltammetric data were carried out using SACMES.[38]

RESULTS AND DISCUSSION

Real-Time Molecular Sensing on Microneedles Irrespective of Target Reactivity. Our first goal was to design integrated devices, allowing rapid testing of microneedle E-AB sensor array performance in vitro. To create our rapid-test devices, we 3D-printed flow cells using biocompatible, methyl methacrylate-based resins (Figure 2A). The main inlet of these devices was connected to a peristaltic pump flowing buffered solutions from a beaker. The solutions overfilled the microneedle chamber and slowly flowed out into two external drains located on the sides of each device and open to an underlying waste beaker. This approach allowed us to mimic excretion kinetics as they would occur in a living rodent by the exit of blood drug levels to urine via the kidneys. Moreover, the flow rate is adjustable, allowing us to test sensor performance under different flow conditions (Figure S2). Two additional, secondary inlets are connected to a computer-controlled syringe pump, enabling us to perform drug injections through one and rapid mixing of drug levels (<10 s) through the other (by pulling liquid out and back in). This mixing rate is analogous to the natural mixing of drugs in the bloodstream of rats, as determined by E-AB measurements.[9]

The microneedle electrode arrays employed during our rapid testing were fabricated via established, previously reported procedures.[27] The devices are produced with high reproducibility (∼90% efficiency after wiring) and contain 16 working, 4 counter, and 1 reference microneedle electrodes. The two-dimensional design for our microneedle substrate, showing electrode connections for single and dual devices, is provided as the Supporting Information (Figure S3). To produce the integrated device (Figure 2A), we glued the microneedle devices to the bottom of our flow platform using insulating epoxy resin. For rapid testing, we produced blunt microneedles (not intended for skin penetration) with a height of ∼2.264 mm and a diameter of ∼170 μm (Figure 2B). Using these microneedles, we built E-ABs via incubation in solutions of blocking alkanethiols and aptamers modified with hexanethiol at the 5′ end and methylene blue at the 3′ end, as it is established in the field.[39]

The sensing performance of microneedle E-AB sensor arrays is identical to that of benchmark E-ABs fabricated on commercial disc electrodes. We demonstrated this by fabricating in parallel tobramycin-binding E-ABs on both microneedle devices and disc macroelectrodes (2 mm in diameter). We selected the tobramycin-binding aptamer for this comparison because it is one of the most studied ones in the E-AB platform.[2,3,8,40] To evaluate sensing performance, we built calibration curves in static, buffered solutions by challenging the E-ABs with increasing concentrations of tobramycin and measuring their response via SWV, at signal-on and signal-off square-wave frequencies of 800 Hz and 150 Hz, respectively. We determined these optimal square-wave frequencies for sensor interrogation via frequency maps (Figure S4) and previous reports.[3] The resulting traces (Figure 2C) were identical between electrode types, achieving the same signal gain and dynamic range irrespective of electrode geometry. The analytical characterization of all E-AB sensors used in this work is included as Table S2 in the Supporting Information.

Microneedle E-AB sensor arrays readily support continuous molecular monitoring in flowing buffered solutions. To demonstrate this capability, we serially interrogated microneedle E-ABs every 4.5 s, while flowing buffer at a rate of 0.66 mL/min. To achieve real-time data processing and visualization, we used SACMES,[38] an open-access Python script previously reported by our group. To emulate an in vivo titration, we injected three target tobramycin concentrations, 250 μM, 600 μM, and 1 mM, after collecting an initial 9 min-long baseline (Figure 2D). We specifically adjusted the injection (0.1 mL/min) and mixing (0.5 mL/min) rates of the syringe pump to emulate a bolus, followed by rapid mixing, so that each injection will display a short-lived target plateau concentration, followed by first-order excretion kinetics. The maximum response of each bolus matched the corresponding gain from the calibration curve in Figure 2C. In addition, we implemented KDMs,[3,8] a strategy that leverages the strong signaling dependence of E-ABs on square-wave frequency to correct for baseline drift in real time. Using SACMES, we subtracted the data collected at 150 Hz from that measured at 800 Hz in real time to achieve the drift-corrected drug profiles shown in Figure 2E. To demonstrate the versatility of our platform, we also functionalized microelectrode arrays with vancomycin-binding aptamers.[41] Vancomycin, a glycopeptide antibiotic heavily in use in the United States,[42] is vastly different in molecular structure from tobramycin ($MW_{vancomycin}$ = 1449.27 g mol^{-1} vs $MW_{tobramycin}$ = 467.5 g mol^{-1}). Our results using this aptamer (Figure S5), which show equivalent performance to the tobramycin measurements (Figure 2D,E), highlight the simplicity with which our platform can be adapted to the monitoring of clinically relevant targets. Example raw voltammograms corresponding to the flow data shown in Figure 2D are included in the Supporting Information as Figure S6.

Multiuse Devices Achieving Highly Reproducible Measurements. One caveat of working with heavily engineered devices such as microneedles for sensor prototyping is the relative high cost of fabricating them as the inherent cost comes from the time it takes to produce each batch of devices. To make our technology development process more convenient and cost-effective, we developed a protocol allowing the reuse of each microneedle device for E-AB prototyping over 3 times without an impact on E-AB signaling (exemplified in Figure S1). The detailed cleaning protocol is described in the Experimental Section and Expanded Methods in the Supporting Information. In brief, we take freshly

https://doi.org/10.1021/acs.analchem.2c00829
Anal. Chem. 2022, 94, 8335−8345

prepared microneedle devices (postmetal deposition) and incubate them in pure ethanol for 10 min. This step removes any gold oxides remaining from the fabrication process according to the relation[37]

$$Au_2O_3 + 3CH_3CH_2OH \rightleftharpoons 2Au + 3CH_3CHO + 3H_2O \quad (1)$$

Next, we perform standard electrochemical cleaning steps, as previously reported[34,39] and described in the Supporting Information. Then, we immerse the microneedles in 600 μL of a 10% commercial gold cleaning solution diluted in water (containing 0.1−1% thiourea and 5−10% sulfuric acid per manufacturer instructions) for 10 s. This solution oxidizes the gold surface according to the following equation[43]

$$Au + 2CS(NH_2)_2 \rightleftharpoons Au(NH_2CSNH_2)^{2+} + e^- \quad (2)$$

Finally, we repeat the electrochemical cleaning steps immediately prior to aptamer deposition. To illustrate the performance of this protocol, we functionalized the same microneedle device with tobramycin-binding aptamer three independent times and performed continuous measurements of tobramycin as in Figure 2D,E. The resulting measurements had a relative standard deviation within ∼10% at any given target concentration (Figure 3A), demonstrating that our cleaning protocol enables reproducible device reuse. In addition, the implementation of KDM (Figure 3B) to correct for drift resulted in drug profiles with relative standard deviations that were ≤10% at tobramycin concentrations <1 mM. In contrast, measurements performed on untreated microneedles (Figure 3C) showed lower signal outputs at equal target concentrations and higher baseline noise. The aptamer packing density was also lower and highly variable between untreated devices (not shown). We anticipate our protocol will translate well to other electrode geometries.

Multiplexed Monitoring of Molecular Targets via Multichannel Devices. The availability of an array of microneedle sensors makes it possible to interrogate elements of the array either simultaneously, individually or in groups, to enable multiplexed sensing. Here, we illustrate multiplexed detection by dividing the microneedle array into two sections. For these demonstrations, we changed the cell design from Figure 2A to support an additional injection line connected to the syringe pump (Figure 4A). We also fabricated microneedle arrays containing a separating wall to allow for independent target challenges or aptamer depositions on the two sections (Figure 4B). The separating wall was detachable and could be removed prior to the deployment of the devices in the target medium.

We first evaluated the ability of dual-chamber microneedle E-AB sensor arrays to support simultaneous interrogation of two independent arrays functionalized with the same aptamer but exposed to different targets. For this purpose, we employed a new aptamer developed by the company Aptamer Group Ltd. (United Kingdom) that binds to irinotecan[44] (Figure 4B), a chemotherapeutic prodrug. When bound to the E-AB sensing interface and functionalized with methylene blue, this aptamer underwent binding-induced eT changes, readily enabling E-AB sensing. Calibration of the resulting E-ABs with irinotecan and its main metabolite, SN-38, showed that the aptamer binds to both with similar affinity but achieves greater gain at every concentration when challenged with irinotecan (green vs purple markers in Figure 4C). Using this calibration, we were able to estimate an apparent dissociation constant of K_D = 723 ± 64 nM based on nonlinear regression of the data to the Langmuir−Hill isotherm (Figure S7). This estimated K_D represents a 2 orders-of-magnitude improvement in irinotecan affinity in PBS relative to irinotecan-binding E-ABs previously reported by Plaxco and colleagues,[45] K_D = 126 ± 24 μM. In addition, our E-ABs did not require codeposition of unstructured DNA strands to achieve dual-frequency sensing (Figure 4C−E).

When we continuously interrogated these E-ABs in dual-chamber microneedle devices and the chambers were simultaneously challenged with either irinotecan or SN-38, we successfully achieved independent monitoring of E-AB gains from both sensing chambers. Following three serial boluses at a 2 μM irinotecan concentration, we observed 100% reproducible signaling responses from chamber 1 (Figure 4D),

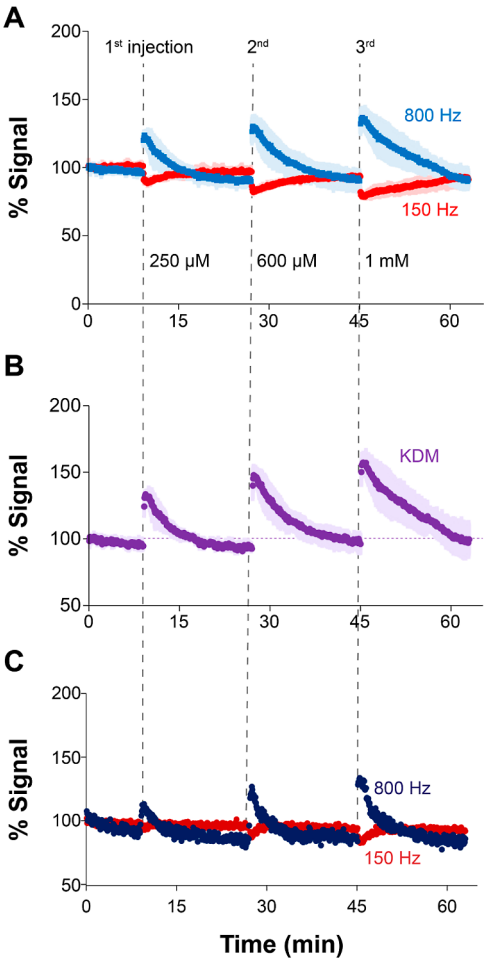

Figure 3. Microneedle arrays can be reused multiple times. The newly developed chemical and electrochemical cleaning protocol reported in this work allows the reuse of microneedle devices multiple times during rapid prototyping and testing. (A) Here, for example, we show the performance of E-ABs fabricated on a single device that was reused three times. The colored data corresponds to the average of three identical measurements performed on the same device after each round of cleaning and functionalization with aptamers. Baseline peak currents at 800 Hz are ∼9 ± 0.5 mA. The shaded areas indicate the standard deviation between measurements. (B) Use of KDM for baseline correction further highlights the reproducibility achieved via the cleaning protocol. (C) For reference, untreated microneedles show lower signal output and higher baseline noise. Baseline peak currents at 800 Hz are ∼1.8 mA, 80% lower than the currents for treated microneedles.

https://doi.org/10.1021/acs.analchem.2c00829
Anal. Chem. 2022, 94, 8335−8345

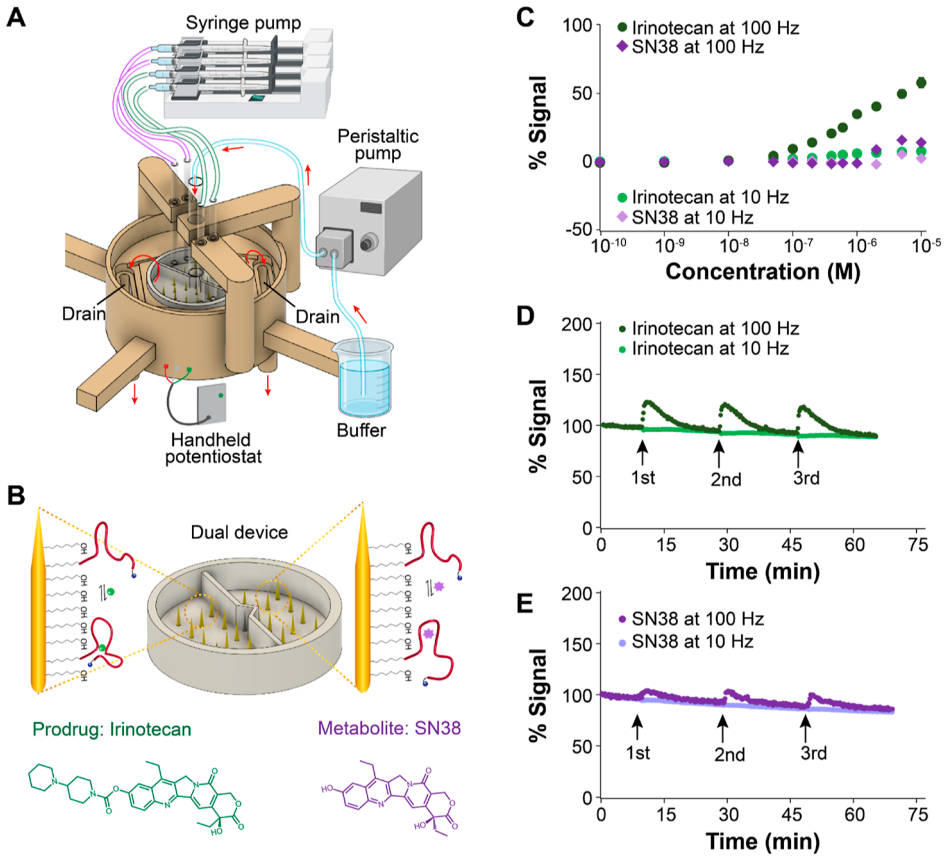

Figure 4. Dual-channel microneedle E-AB devices enable simultaneous evaluation of aptamer specificity. (A) Different from Figure 2A, the 3D-printed cell was adapted to have two separate injection lines at opposite sides of the central support. By connecting these lines to the syringe pump, we could automatically inject and mix the prodrug irinotecan and its major metabolite SN-38 in the left and right chambers, respectively. (B) We functionalized the microneedles in both chambers with irinotecan-binding aptamers. In the presence of irinotecan, the E-AB sensors undergo binding-induced changes in eT between the reporter and the microneedles. However, the metabolite SN-38 induces minor conformational changes relative to irinotecan binding. (C) Microneedle E-AB sensor arrays display higher signal gain when challenged with irinotecan than with the metabolite SN-38 at square-wave frequencies of 100 Hz. (D) Demonstration of continuous, reproducible irinotecan monitoring following three boluses at a target concentration of 2 μM irinotecan in the left chamber. (E) Similarly, when challenging the right chamber with the metabolite SN-38, lower gains were obtained following three serial boluses. Voltammetric measurements were performed every 11 s in 20 mM phosphate solution containing 137 mM NaCl, 2.7 mM KCl, 2 mM $MgCl_2$, and 1 mM $CaCl_2$ (pH = 6.0).

similar in magnitude to the gain observed in our calibration curve for the matching 2 μM concentration (Figure 4C). Likewise, the response to 2 μM SN-38 additions performed in chamber 2 showed excellent repeatability but lower gain (Figure 4E), also in agreement with our calibration data. Example raw voltammograms corresponding to the flow data shown in Figure 4D,E are included in the Supporting Information as Figures S8 and S9. These results illustrate the versatility of the microneedle E-AB sensor array platform, which can be easily fabricated with different configurations to allow simultaneous and multiplexed evaluation of aptamer selectivity.

We next evaluated the ability of dual-chamber microneedle E-AB sensor arrays to support simultaneous interrogation of two independent arrays each functionalized with a different aptamer. For this demonstration, we employed the same flow device illustrated in Figure 4A, except that this time, one of the microneedle array chambers was functionalized with the irinotecan-binding aptamer and the other with a doxorubicin-binding aptamer[8] (Figure 5A). Doxorubicin is a chemotherapeutic regularly used for the treatment of certain leukemias and Hodgkin's lymphoma.[46−48] The idea was to demonstrate the concept that a microneedle E-AB sensor array could be used to simultaneously monitor an array of chemotherapeutic agents, providing an unparalleled route for therapeutic drug monitoring during cancer treatment. We note, however, that irinotecan and doxorubicin are never dosed together; thus, our demonstration here is purely conceptual. Future development of aptamers binding to, for example, fluorouracil, could generate a strong matching pair for irinotecan since these therapeutics are used in combination therapy.[49] Similarly, doxorubicin is often codosed with cyclophosphamide or Taxotere;[50,51] thus, developing aptamers against these targets could result in functional dual devices for chemotherapy monitoring. However, the development of such aptamers is beyond the scope of this work. Instead, the conceptual demonstration we present here aims to highlight the versatility of our microneedle sensor platform to achieve multiplexed monitoring of therapeutic agents.

Following dual-chamber E-AB sensor fabrication, we calibrated doxorubicin aptamer-based sensors by challenging the sensors with increasing concentrations of doxorubicin, respectively (Figure 5B). Doing this, we determined an apparent dissociation constant for the doxorubicin aptamer of K_D = 969 ± 170 nM (Figure S7), in close agreement with the aptamer's affinity as first reported by Soh and colleagues

https://doi.org/10.1021/acs.analchem.2c00829
Anal. Chem. 2022, 94, 8335−8345

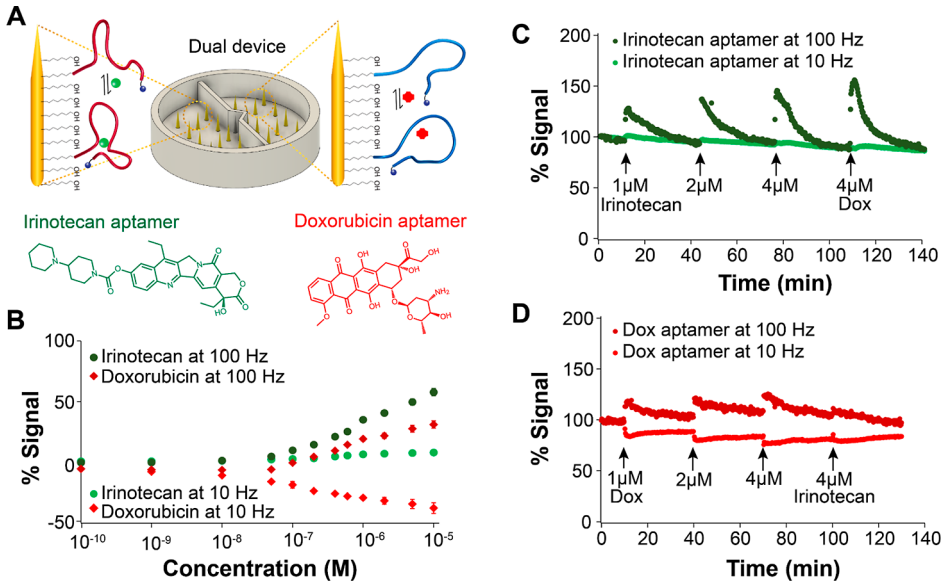

Figure 5. Dual-channel microneedle E-AB devices enable multiplexed sensing. (A) We functionalized the microneedles in each chamber with either irinotecan-binding or doxorubicin-binding aptamers. (B) Mean calibration curves of six irinotecan-binding and doxorubicin-binding E-ABs obtained using commercial disc macroelectrodes (2 mm in diameter) demonstrate that both sensors showed high affinity when challenged with their targets. (C) When simultaneously injecting irinotecan and doxorubicin in either chamber of the microneedle device, it was possible to successfully monitor E-AB signals induced by target binding to the respective E-ABs. In the case of the irinotecan-binding sensor, irinotecan boluses of increasing concentrations produced corresponding E-AB responses. Challenging the same E-ABs with doxorubicin, a known DNA intercalator, also produced large signal changes. (D) Likewise, challenging the doxorubicin-binding E-ABs with doxorubicin boluses of increasing concentration caused proportional E-AB responses. Challenging these sensors with 4 μM irinotecan did not induce E-AB signal changes. Voltammetric measurements were performed every 12 s in 20 mM phosphate, 137 mM NaCl, 2.7 mM KCl, 2 mM $MgCl_2$, and 1 mM $CaCl_2$ (pH = 6.0).

(824 ± 18 nM).[8] When we continuously interrogated these dual-chamber microneedle devices and the chambers were simultaneously challenged with either irinotecan or doxorubicin, we successfully achieved independent monitoring of the two drugs. For the case of irinotecan, we observed sharp responses following boluses at 1, 2, and 4 μM irinotecan (Figure 5C), with signaling that, again, matched our calibration curve (Figure 5B) and returned to the baseline. For doxorubicin, in contrast, we observed E-AB responses to each bolus, but the return to the baseline was not complete between target injections (Figure 5D). This effect is potentially due to doxorubicin nonspecifically binding to the plastic walls of our flow devices and slowly leaching back into the solution during the flow experiment. We do not foresee this problem happening when deploying our devices in vivo since all plastic walls will be removed for such applications. In addition, plastic surfaces in contact with doxorubicin could be pretreated with surfactants to prevent nonspecific drug binding. Example raw voltammograms corresponding to the flow data shown in Figure 5C,D are included in the Supporting Information as Figures S10 and S11.

The selectivity of microneedle E-AB sensor arrays is, of course, limited by the selectivity of the parent aptamers used to fabricate the sensors and the nature of the targets. Doxorubicin, for example, is a known DNA intercalator that can bind to any double-stranded DNA. Because both aptamers used in this work present self-complementarity within their sequences and some secondary structure (i.e., double-stranded character), doxorubicin can bind both. We confirmed this in our flow experiments by injecting doxorubicin into the chamber containing the irinotecan-binding E-ABs and observing a sharp response to the drug injection (last bolus in Figure 5C). In contrast, irinotecan is not an intercalation agent. Its mechanism of action is based on specific binding to the topoisomerase I−DNA complex, forming a tertiary structure that prevents replication in cancer cells.[52] As such, injection of irinotecan into the chamber containing doxorubicin-binding E-ABs resulted in minimal response to the drug addition (last bolus in Figure 5D). Overall, these results highlight the potential of microneedle E-AB sensors to enable simultaneous and multiplexed monitoring of therapeutic agents in real time.

Wearable, Continuous, and Real-Time Molecular Monitoring in Vivo. Microneedle E-AB sensor arrays can readily enable continuous molecular monitoring in vivo. We illustrate this capability here by deploying one microneedle E-AB sensor array on the skin of an anesthetized rat and performing continuous monitoring of the antibiotic tobramycin following IV dosing (Figure 6). We note that the goal of this work was to qualitatively probe whether our microneedle E-AB sensor arrays could support continuous molecular monitoring in vivo, with no goal of performing quantitative or detailed pharmacokinetic measurements at this time. Such efforts will be devoted to future work. For our in vivo measurements, we fabricated new devices devoid of chamber walls and containing smaller microneedles: 170 μm in diameter, a sharp tip end (<20 μm), and 1.1 mm tall (Figure 6A). The electronics behind these devices were encased inside a 3D-printed plastic chamber for convenience (Figure 6B). We placed them onto the shaved skin of rodents by applying a pressure similar in force to a normal handshake and fixed them in place via medical grade tape (not shown). Visual inspection of the deployment site post measurements revealed the correct microwound pattern expected from the microneedle array (Figure 6C). To confirm penetration through the epidermis and into the dermis of the animal where ISF is found, we

https://doi.org/10.1021/acs.analchem.2c00829
Anal. Chem. 2022, 94, 8335−8345

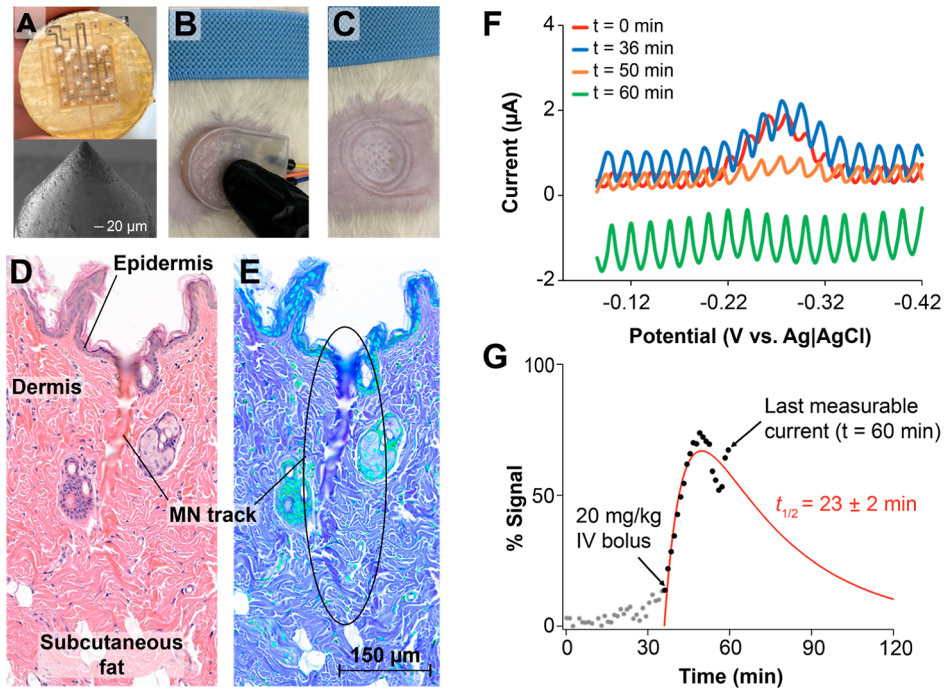

Figure 6. Continuous molecular monitoring of tobramycin concentration in ISF. Proof-of-concept monitoring of tobramycin levels in the dermis of one rat following IV administration of the drug at a dose of 20 mg/kg. (A) We fabricated sharper microneedles that were 150 μm in diameter and 1.1 mm in length. (B) The microneedles were placed on the freshly shaved abdomen of one male rat. (C) Removal of the device from the skin revealed the expected pattern of micropunctures. (D) H&E-stained skin tissue illustrating different histological features of the rat's skin and one penetrating track left after insertion of the microneedles. (E) Hue- and contrast-adjusted duplicate image highlighting the track mark after microneedle removal. (F) Although noisy, electrochemical interrogation of the microneedle array resulted in discernible square-wave voltammograms in ISF that strongly responded to tobramycin following an IV bolus injected into the right jugular vein of the rat (drop from blue to orange). (G) Real-time processing of the voltammograms using SACMES allowed us to visualize the sensor response, here plotted as relative signal after tobramycin dosing. SACMES uses rolling average and polynomial fit algorithms to remove noise from voltammograms, thus enabling the extraction of high signal-to-noise E-AB data. Unfortunately, progressive degradation of the sensors in ISF made it impossible to distinguish signals past t = 60 min. The red line shows a regression analysis to a two-compartment drug absorption pharmacokinetic model using the data points available.

dissected the skin tissue post measurements, fixed it in *p*-formaldehyde, and performed histological H&E staining to reveal microneedle tracks (Figure 6D). We note that the fixation and staining protocols strongly dehydrate the tissues, thereby collapsing the microneedle tracks into smaller dimensions than those expected based on physical measurements via scanning electron microscopy (Figure 6A). Nevertheless, we were able to observe clear penetrating tracks with breakage of the epidermis and an approximate length of 500 μm and width of 50 μm. The contrast- and hue-adjusted duplicate image shown in Figure 6E is included to facilitate observation of the penetrating tracks of the microneedle.

The skin-worn microneedle sensor arrays successfully achieved continuous molecular measurements in ISF. We demonstrate this by serially interrogating one tobramycin-binding microneedle E-AB sensor array via voltammetry while placed on the skin of a rat. We timed the voltammetric sweeps 70 s apart to minimize sensor drift[40,53], and interrogated at square-wave frequencies of 80, 150, 200, and 240 Hz. Unfortunately, the noise level at frequencies higher than 80 Hz was larger in magnitude than the redox wave from the aptamer-bound reporters, thus precluding the use of KDM in this measurement. However, measurements at 80 Hz produced clear voltammograms that could be processed in real time using SACMES.[38] At this frequency, tobramycin-binding E-ABs behaved as signal-off sensors in ISF, responding to increases in drug concentration with corresponding decreases in voltammetric current (Figure 6F). When processing the data in real time, we observed a sudden change in current at the exact time of tobramycin IV dosing (Figure 6G). Even though the skin dermis is a separate compartment from systemic blood, it is highly perfused, and thus, we expected the two compartments to rapidly equilibrate molecular concentrations. In agreement with this, our sensor showed a rapid absorption phase immediately following IV dosing of tobramycin. This phase was succeeded by a short-lived plateau and the beginning of signal decay in response to drug excretion kinetics. Unfortunately, we could not fully resolve the elimination phase of the drug before the sensor signal decayed below noise level due to sensor degradation (green trace in Figure 6F). However, performing regression analysis of the points collected against a two-compartment drug adsorption model resulted in an elimination half-life of 23 ± 2 min, which is in close agreement with the previous E-AB measurements of plasma tobramycin excretion kinetics.[4] Building upon these encouraging in vivo results, we will focus future efforts on mitigating the environmental noise seen in our voltammetric measurements and extending the operational life of our sensors in vivo.

CONCLUSIONS

We report the coupling of E-AB sensors with microneedle electrode arrays to demonstrate continuous molecular monitoring. Because aptamer-based sensors achieve molecular

https://doi.org/10.1021/acs.analchem.2c00829
Anal. Chem. 2022, 94, 8335−8345

recognition via reversible affinity interactions and not reactivity with the target, they offer the possibility to expand the molecular targets that can be sensed beyond the electrocatalytic and enzymatic detection of redox-active molecules. This work demonstrates examples of single and multiplexed molecular measurements achieved via mono- and dual-channel devices. However, the possibility to interrogate individual microneedle electrodes within a large array also exists, potentially allowing for simultaneous multichannel interrogation of a library of molecular targets. In addition, this work shows that 3D printed, gold-coated microneedle electrode arrays can be easily functionalized with E-AB sensing chemistries to enable molecular monitoring in the ISF of research animals. Future demonstrations of the technology will focus on implementing noise reduction and enhanced stability strategies to allow for high-resolution in vivo measurements. We will also devote future efforts to test the resiliency to skin penetration and biocompatibility of in vivo microneedle E-AB sensor arrays.

■ ASSOCIATED CONTENT

Supporting Information

The Supporting Information is available free of charge at https://pubs.acs.org/doi/10.1021/acs.analchem.2c00829.

Expanded Methods cleaning protocol monitoring) and additional data (PDF)

■ AUTHOR INFORMATION

Corresponding Authors

Joseph Wang − *Department of Nanoengineering, University of California San Diego, La Jolla, California 92093, United States*; Email: josephwang@ucsd.edu

Netzahualcóyotl Arroyo-Currás − *Department of Pharmacology and Molecular Sciences and Biochemistry, Cellular and Molecular Biology, Johns Hopkins University School of Medicine, Baltimore, Maryland 21202, United States*; orcid.org/0000-0002-2740-6276; Email: netzarroyo@jhmi.edu

Authors

Yao Wu − *Department of Pharmacology and Molecular Sciences, Johns Hopkins University School of Medicine, Baltimore, Maryland 21202, United States*; orcid.org/0000-0003-1296-6569

Farshad Tehrani − *Department of Nanoengineering, University of California San Diego, La Jolla, California 92093, United States*

Hazhir Teymourian − *Department of Nanoengineering, University of California San Diego, La Jolla, California 92093, United States*; orcid.org/0000-0003-0025-4732

John Mack − *Biochemistry, Cellular and Molecular Biology, Johns Hopkins University School of Medicine, Baltimore, Maryland 21202, United States*

Alexander Shaver − *Department of Pharmacology and Molecular Sciences, Johns Hopkins University School of Medicine, Baltimore, Maryland 21202, United States*; orcid.org/0000-0002-5478-5291

Maria Reynoso − *Department of Nanoengineering, University of California San Diego, La Jolla, California 92093, United States*

Jonathan Kavner − *Department of Nanoengineering, University of California San Diego, La Jolla, California 92093, United States*

Nickey Huang − *Department of Nanoengineering, University of California San Diego, La Jolla, California 92093, United States*

Allison Furmidge − *Department of Nanoengineering, University of California San Diego, La Jolla, California 92093, United States*

Andrés Duvvuri − *Department of Nanoengineering, University of California San Diego, La Jolla, California 92093, United States*

Yuhang Nie − *Department of Nanoengineering, University of California San Diego, La Jolla, California 92093, United States*

Lori M. Laffel − *Joslin Diabetes Center, Harvard Medical School, Boston, Massachusetts 02215, United States*

Francis J. Doyle III − *Harvard John A. Paulson School of Engineering and Applied Sciences, Harvard University, Allston, Massachusetts 02134, United States*

Mary-Elizabeth Patti − *Joslin Diabetes Center, Harvard Medical School, Boston, Massachusetts 02215, United States*

Eyal Dassau − *Harvard John A. Paulson School of Engineering and Applied Sciences, Harvard University, Allston, Massachusetts 02134, United States*

Complete contact information is available at: https://pubs.acs.org/10.1021/acs.analchem.2c00829

Author Contributions

Y.W. and J.M. fabricated all E-AB sensors and tested them in vitro. F.T. designed all microneedle devices. H.T., M.R., J.K., N.H., A.F., A.D., and Y.N. contributed to the fabrication of both in vitro and in vivo microneedle devices. A.S. performed all animal surgeries and in vivo E-AB trials. J.W. and N.A.C. collaboratively designed the experiments with Y.W. and F.T. and supervised the development of the work. L.M.L., F.J.D., E.D., and M.E.P. analyzed data and contributed to the writing of the manuscript. All authors contributed to the writing of the final version of this manuscript.

Notes

The authors declare the following competing financial interest(s): E.D. reports receiving grants from JDRF, NIH, and Helmsley Charitable Trust, personal fees from Roche and Eli Lilly, patents on artificial pancreas technology, and product support from Dexcom, Insulet, Tandem, and Roche. E.D. is currently an employee and shareholder of Eli Lilly and Company. The work presented in this manuscript was performed as part of his academic appointment and is independent of his employment with Eli Lilly and Company.F.J.D. reports equity, licensed IP and is a member of the Scien-tific Advisory Board of Mode AGC.L.M.L. reports grant support to her institution from NIH, JDRF, Helmsley Charitable Trust, Eli Lilly and Company, Insulet, Dexcom, and Boehringer Ingelheim; she receives con-sulting fees unrelated to the current report from NovoNordisk, Roche, Dexcom, Insulet, Boehringer Ingelheim, Medtronic, Dompe, and Provention. M.E.P. reports receiving grant support, provided to her institution, from NIH, Helmsley Charitable Trust, Chan Zuckerberg Foundation, and Dexcom, patents related to hypoglycemia and pump therapy for hypoglycemia, and advisory board fees from Fractyl (unrelated to the current

https://doi.org/10.1021/acs.analchem.2c00829
Anal. Chem. 2022, 94, 8335−8345

report).F.T., H.T., E.D., J.W. and N.A.C. are co-inventors of patents filed based on the work reported in this study.

■ ACKNOWLEDGMENTS

This work was supported by The Leona M. and Harry B. Helmsley Charitable Trust under award number 7505508-5108014 (2018PG-TI0061).

■ REFERENCES

(1) Teymourian, H.; Parrilla, M.; Sempionatto, J. R.; Montiel, N. F.; Barfidokht, A.; Van Echelpoel, R.; De Wael, K.; Wang, J. *ACS Sens.* **2020**, *5*, 2679−2700.
(2) Arroyo-Currás, N.; Ortega, G.; Copp, D. A.; Ploense, K. L.; Plaxco, Z. A.; Kippin, T. E.; Hespanha, J. P.; Plaxco, K. W. *ACS Pharmacol. Transl. Sci.* **2018**, *1*, 110−118.
(3) Arroyo-Currás, N.; Somerson, J.; Vieira, P. A.; Ploense, K. L.; Kippin, T. E.; Plaxco, K. W. *Proc. Natl. Acad. Sci. U.S.A.* **2017**, *114*, 645−650.
(4) Vieira, P. A.; Shin, C. B.; Arroyo-Currás, N.; Ortega, G.; Li, W.; Keller, A. A.; Plaxco, K. W.; Kippin, T. E. *Front. Mol. Biosci.* **2019**, *6*, 69.
(5) Wolkowicz, K. L.; Aiello, E. M.; Vargas, E.; Teymourian, H.; Tehrani, F.; Wang, J.; Pinsker, J. E.; Doyle, F. J., 3rd; Patti, M. E.; Laffel, L. M.; Dassau, E. *Bioeng. Transl. Med.* **2021**, *6*, No. e10201.
(6) Aiello, E. M.; Deshpande, S.; Özaslan, B.; Wolkowicz, K. L.; Dassau, E.; Pinsker, J. E.; Doyle, F. J. *Curr. Opin. Biomed. Eng.* **2021**, *19*, 100312.
(7) Li, J.; Liang, J. Y.; Laken, S. J.; Langer, R.; Traverso, G. *Trends Chem.* **2020**, *2*, 319−340.
(8) Ferguson, B. S.; Hoggarth, D. A.; Maliniak, D.; Ploense, K.; White, R. J.; Woodward, N.; Hsieh, K.; Bonham, A. J.; Eisenstein, M.; Kippin, T. E.; Plaxco, K. W.; Soh, H. T. *Sci. Transl. Med.* **2013**, *5*, 213ra165.
(9) Arroyo-Currás, N.; Dauphin-Ducharme, P.; Ortega, G.; Ploense, K. L.; Kippin, T. E.; Plaxco, K. W. *ACS Sens.* **2018**, *3*, 360−366.
(10) Falagas, M. E.; Karageorgopoulos, D. E. *Lancet* **2010**, *375*, 248−251.
(11) Shuter, B.; Aslani, A. *Eur. J. Appl. Physiol.* **2000**, *82*, 250−254.
(12) Neely, M. N.; Kato, L.; Youn, G.; Kraler, L.; Bayard, D.; van Guilder, M.; Schumitzky, A.; Yamada, W.; Jones, B.; Minejima, E. *Antimicrob. Agents Chemother.* **2018**, *62*, No. e02042.
(13) Zhang, T.; Cai, S.; Forrest, W. C.; Mohr, E.; Yang, Q.; Forrest, M. L. *Appl. Spectrosc.* **2016**, *70*, 1529−1536.
(14) Zhong, X.; Tong, X.; Ju, Y.; Du, X.; Li, Y. *Curr. Drug Metab.* **2018**, *19*, 1152−1158.
(15) Payne, K. D.; Hall, R. G. *Expert Rev. Anti-Infect. Ther.* **2014**, *12*, 829−854.
(16) Tran, B. Q.; Miller, P. R.; Taylor, R. M.; Boyd, G.; Mach, P. M.; Rosenzweig, C. N.; Baca, J. T.; Polsky, R.; Glaros, T. *J. Proteome Res.* **2018**, *17*, 479−485.
(17) Samant, P. P.; Niedzwiecki, M. M.; Raviele, N.; Tran, V.; Mena-Lapaix, J.; Walker, D. I.; Felner, E. I.; Jones, D. P.; Miller, G. W.; Prausnitz, M. R. *Sci. Transl. Med.* **2020**, *12*, No. eaaw0285.
(18) Siegmund, T.; Heinemann, L.; Kolassa, R.; Thomas, A. *J. Diabetes Sci. Technol.* **2017**, *11*, 766−772.
(19) Teymourian, H.; Tehrani, F.; Mahato, K.; Wang, J. *Adv. Healthcare Mater.* **2021**, *10*, No. e2002255.
(20) Miller, P. R.; Taylor, R. M.; Tran, B. Q.; Boyd, G.; Glaros, T.; Chavez, V. H.; Krishnakumar, R.; Sinha, A.; Poorey, K.; Williams, K. P.; Branda, S. S.; Baca, J. T.; Polsky, R. *Commun. Biol.* **2018**, *1*, 173.
(21) van der Maaden, K.; Jiskoot, W.; Bouwstra, J. *J. Controlled Release* **2012**, *161*, 645−655.
(22) Singh, P.; Carrier, A.; Chen, Y.; Lin, S.; Wang, J.; Cui, S.; Zhang, X. *J. Controlled Release* **2019**, *315*, 97−113.
(23) Goud, K. Y.; Moonla, C.; Mishra, R. K.; Yu, C.; Narayan, R.; Litvan, I.; Wang, J. *ACS Sens.* **2019**, *4*, 2196−2204.
(24) Mohan, A. M. V.; Windmiller, J. R.; Mishra, R. K.; Wang, J. *Biosens. Bioelectron.* **2017**, *91*, 574−579.
(25) Mishra, R. K.; Vinu Mohan, A. M.; Soto, F.; Chrostowski, R.; Wang, J. *Analyst* **2017**, *142*, 918−924.
(26) Windmiller, J. R.; Valdés-Ramírez, G.; Zhou, N.; Zhou, M.; Miller, P. R.; Jin, C.; Brozik, S. M.; Polsky, R.; Katz, E.; Narayan, R.; Wang, J. *Electroanalysis* **2011**, *23*, 2302−2309.
(27) Teymourian, H.; Moonla, C.; Tehrani, F.; Vargas, E.; Aghavali, R.; Barfidokht, A.; Tangkuaram, T.; Mercier, P. P.; Dassau, E.; Wang, J. *Anal. Chem.* **2020**, *92*, 2291−2300.
(28) Mishra, R. K.; Goud, K. Y.; Li, Z.; Moonla, C.; Mohamed, M. A.; Tehrani, F.; Teymourian, H.; Wang, J. *J. Am. Chem. Soc.* **2020**, *142*, 5991−5995.
(29) Xiao, Y.; Lubin, A. A.; Heeger, A. J.; Plaxco, K. W. *Angew. Chem., Int. Ed.* **2005**, *44*, 5456−5459.
(30) Tuerk, C.; Gold, L. *Science* **1990**, *249*, 505−510.
(31) Ellington, A. D.; Szostak, J. W. *Nature* **1990**, *346*, 818−822.
(32) Wu, Y.; Belmonte, I.; Sykes, K. S.; Xiao, Y.; White, R. J. *Anal. Chem.* **2019**, *91*, 15335−15344.
(33) Yi, K.; Wang, Y.; Shi, K.; Chi, J.; Lyu, J.; Zhao, Y. *Biosens. Bioelectron.* **2021**, *190*, 113404.
(34) Shaver, A.; Curtis, S. D.; Arroyo-Currás, N. *ACS Appl. Mater. Interfaces* **2020**, *12*, 11214−11223.
(35) Arroyo-Currás, N.; Dauphin-Ducharme, P.; Scida, K.; Chávez, J. L. *Anal. Methods* **2020**, *12*, 1288−1310.
(36) Dauphin-Ducharme, P.; Ploense, K. L.; Arroyo-Currás, N.; Kippin, T. E.; Plaxco, K. W. Electrochemical aptamer-based sensors: A platform approach to high-frequency molecular monitoring in situ in the living body. *Biomedical Engineering Technologies*; Methods in Molecular Biology; Ossandon, M. R., Baker, H., Rasooly, A., Eds.; Springer US: Humana, New York, NY, 2022; Vol. *2393*, pp 479−492.
(37) Carvalhal, R. F.; Sanches Freire, R.; Kubota, L. T. *Electroanalysis* **2005**, *17*, 1251−1259.
(38) Curtis, S. D.; Ploense, K. L.; Kurnik, M.; Ortega, G.; Parolo, C.; Kippin, T. E.; Plaxco, K. W.; Arroyo-Currás, N. *Anal. Chem.* **2019**, *91*, 12321−12328.
(39) Xiao, Y.; Lai, R. Y.; Plaxco, K. W. *Nat. Protoc.* **2007**, *2*, 2875−2880.
(40) Pellitero, M. A.; Curtis, S. D.; Arroyo-Currás, N. *ACS Sens.* **2021**, *6*, 1199−1207.
(41) Dauphin-Ducharme, P.; Yang, K.; Arroyo-Currás, N.; Ploense, K. L.; Zhang, Y.; Gerson, J.; Kurnik, M.; Kippin, T. E.; Stojanovic, M. N.; Plaxco, K. W. *ACS Sens.* **2019**, *4*, 2832−2837.
(42) Dilworth, T. J.; Schulz, L. T.; Rose, W. E. *Clin. Infect. Dis.* **2021**, *72*, E675−E681.
(43) Groenewald, T. *Hydrometallurgy* **1976**, *1*, 277−290.
(44) Puscasu, A.; Zanchetta, M.; Posocco, B.; Bunka, D.; Tartaggia, S.; Toffoli, G. *Anal. Bioanal. Chem.* **2021**, *413*, 1225−1236.
(45) Idili, A.; Arroyo-Currás, N.; Ploense, K. L.; Csordas, A. T.; Kuwahara, M.; Kippin, T. E.; Plaxco, K. W. *Chem. Sci.* **2019**, *10*, 8164−8170.
(46) Chand, V. K.; Link, B. K.; Ritchie, J. M.; Shannon, M.; Wooldridge, J. E. *Leuk. Lymphoma* **2006**, *47*, 657−663.
(47) Pérez-Blanco, J. S.; Santos-Buelga, D.; Fernández de Gatta, M. d. M.; Hernández-Rivas, J. M.; Martín, A.; García, M. J. *Br. J. Clin. Pharmacol.* **2016**, *82*, 1517−1527.
(48) Zhou, T.; Shen, Q.; Peng, H.; Chao, T.; Zhang, L.; Huang, L.; Yang, K.; Thapa, S.; Yu, S.; Jiang, Y. *Ann. Hematol.* **2018**, *97*, 141−147.
(49) Harris, S. M.; Mistry, P.; Freathy, C.; Brown, J. L.; Charlton, P. A. *Br. J. Cancer* **2005**, *92*, 722−728.
(50) Torrisi, R.; Orlando, L.; Ghisini, R.; Veronesi, P.; Intra, M.; Rocca, A.; Balduzzi, A.; Cardillo, A.; Goldhirsch, A.; Colleoni, M. *Anticancer Res.* **2006**, *26*, 3861−3864.
(51) Oakman, C.; Francis, P. A.; Crown, J.; Quinaux, E.; Buyse, M.; De Azambuja, E.; Margeli Vila, M.; Andersson, M.; Nordenskjöld, B.; Jakesz, R.; Thürlimann, B.; Gutiérrez, J.; Harvey, V.; Punzalan, L.; Dell'orto, P.; Larsimont, D.; Steinberg, I.; Gelber, R. D.; Piccart-Gebhart, M.; Viale, G.; Di Leo, A. *Ann. Oncol.* **2013**, *24*, 1203−1211.
(52) Bailly, C. *Curr. Med. Chem.* **2000**, *7*, 39−58.

https://doi.org/10.1021/acs.analchem.2c00829
Anal. Chem. 2022, 94, 8335−8345

(53) Leung, K. K.; Downs, A. M.; Ortega, G.; Kurnik, M.; Plaxco, K. W. *ACS Sens.* **2021**, *6*, 3340−3347.

NOTE ADDED AFTER ASAP PUBLICATION

This paper was originally published ASAP on June 2, 2022, with an error in Figure 6G. The corrected version was reposted on June 3, 2022.

https://doi.org/10.1021/acs.analchem.2c00829
Anal. Chem. 2022, 94, 8335−8345